Numerical investigation of the slipstream characteristics of a maglev train in a tunnel

Liu, Zhen; Zhou, Dan; Soper, David; Chen, Guang; Hemida, Hassan; Guo, Zijian; Li, Xianli

DOI:
10.1177/09544097221100658

Numerical investigation of the slipstream characteristics of a maglev train in a tunnel

Zhen Liu[2], Dan Zhou[1]*, David Soper[2], Guang Chen[1], Hassan Hemida[2], Zijian Guo[2], Xianli Li[1]

Key Laboratory of Traffic Safety on Track of Ministry of Education, School of Traffic & Transportation Engineering, Central South University, Changsha 410075, PR China

School of Civil Engineering, University of Birmingham, Birmingham, UK

ABSTRACT: High-speed maglev trains operate at higher speeds than conventional high-speed trains. This has implications on intensified aerodynamic issues, such as the transition between open air running and entering into a tunnel. In this paper, numerical simulation of a maglev train entering a tunnel is carried out using IDDES methods (based on SST k-omega model) to analyze the changing slipstream. The peaks and fluctuations of the slipstream are analyzed, together with the transient wake characteristics and TKE (turbulent kinetic energy) distributions. The influence of train nose length on the slipstream and its associated characteristics inside tunnels is also investigated in this paper. It was found that as the maglev train enters the tunnel, the wake slipstream at measuring points close to tunnel entrance increases significantly then decreases slightly with the increase of distance to tunnel entrance. Overall, the fluctuation and magnitude of slipstream inside tunnel is larger than that on open line, more specifically, the maximum TKE generated inside tunnel is. 7.62% larger than that on the open line at contour X=3H behind the train tail. Besides it takes longer time for the slipstream inside tunnel to return to the initial condition. These phenomena could be explained by that the scale of vortex structure formed behind the train tail is larger, the developing distance of the wake vortices in the streamwise direction is longer and the TKE generated is more significant inside tunnel. It was also found that increasing the nose length could effectively decrease the spatial scale and TKE of the wake vortices, which resulted on reducing the peak and pulsation of wake slipstream. Comparing to that of 5.4m, the peak of the wake slipstream of the maglev trains with the 7.4m and 9.4m nose lengths at Y = 0.235m(0.385) is reduced by approximately 23.7%(58%) and 35.9%(82.2%) on open field, and by about 3.6%(4.7%) and 14%(18.5%) inside tunnel. Besides, the maximum TKE at contour X=2H/3H/5H behind the train tail decreases about 14.4%/10.7%/11.3% and 51%/31.5%/18% as the nose length increase to 7.4m and 9.4m respectively.

1 Introduction

Compared with conventional high-speed trains, the maglev train completely eliminates the adverse

*Corresponding author: Dan Zhou

E-mail address: zd_lzj@126.com

effects caused by wheel-rail contact, which greatly raises the opportunity for higher operating speeds. In recent years, research on maglev systems have been carried out mainly in China, Japan, Germany, USA and other countries, with a view to trial operation lines under construction or recently opened. Due to the environmental limitations and the requirement to achieve the desired operation speed, it typically required that up to 50% of a journey to be within a tunnel. [1]For example, the central Shinkansen project in Japan, started in 2013, includes a tunnel length of 24.6km, and the total proportion of the line in a tunnel totals 86%. However, it is known that train aerodynamic problems are intensified in tunnel, due to the relative confinement, including the increasing slipstream magnitude that could cause damage to tunnel infrastructures and danger to trackside workers.

Train slipstream are formed by the movement of a train through the air as the surrounding flow moves with the train due to viscosity. [2,3]According to previous research, the slipstream of a high speed train (HST) operating on open line has a typical profile including a nose region (upstream and nose region), boundary-layer region and wake region (near-wake and far-wake region).[4,5,6] The near-wake region is dominated by an unsteady gust peak created by a pair of counter-rotating vortices, which brings the major adverse effect and receives special attention from researchers. A great number of experiments and numerical simulations has been done to investigate the characteristics of the vortex street (frequency, length scale, motion, etc.) and slipstream profile of HST, passenger train and freight trains operating on open field.[3,7,8,9,10,11,12] Results indicated that the characteristic large-scale vortex structure varies from train-to-train due to a sensitive to the shape of tail train, as well as being influenced by the track as it extends.[3,5,13] Besides, the instantaneous flow structure and aerodynamic performance of high-speed trains under cross-wind are also been widely investigated [14,15,16]. The influence of geometry of the train and objects around the train (e.g. train nose shapes, shelters, windbreaks, air fences) on the distribution of velocity and the characteristics of the vortices are further investigated[17,18,19,20]. Maglev trains operate at high train speeds, with the track positioned relatively high above the ground and there isn't any bogies which is different from other trains. However, few investigation have been done to investigate the slipstream behaviour and vortices generated by maglev trains.

The flow inside tunnels is more unsteady and turbulent than that around trains in open air.[21,22] In addition, the velocity around trains in tunnels increases due to the piston effect. Full-scaled experiments and moving model rig tests (MMR) have been carried out to assess the slipstream development of a HST in a tunnel or confined space.[23,24] Results indicated that the gust peak is proportional to operating speed and related to train and tunnel length, shape of train end and blockage ratio. It has also been noted that it takes a longer time for the air inside a tunnel to return to initial condition comparing to that on open line. CFD simulations have also been carried out, mainly using RANS (Reynolds-averaged Naiver-Stokes) methods due to the large computational resource required to simulate a moving train.[25,26,27,28] However, URANS has its limitations to measure highly turbulent slipstreams quantitatively since it fails to predict the developing of vortices and the correlated dynamic response,[29] which the DES or LES methods are capable of doing. With the development of computational capability, Khayrullina[30] simulated trains passing through a platform using LES method. The wind conditions when the train enter and exit the platform is analysed to assess its hazard to objects and passengers on the platform. Though these researches show that the slipstream yields a much larger magnitude peak value in a tunnel, little is known for the fundamentals of its formation and whether the assessment for slipstream in open field[31] is suitable for that in confined spaces[24,25].

Since the wake flow structures formed by the separation of boundary layer at train tail have significant impact on wake gust, efforts have been made to reduce the adverse effect of the slipstream by optimizing the train nose shape. The results of Bell, et al[13] showed that the angle of the roof influences the separation of the tail train surface and further induces vortices of different dominating frequencies and length scale. As a result, a shorter nose leads to thicker boundary layer at train tail, higher slipstream peak and more vortex structures in the wake.[2,32,33,34] More specifically, Chen[2] and Li[34] investigated the effect of nose length on slipstream development quantitively by comparing the "characteristic velocity" defined by Technical Specifications for Interoperability (TSI)[31], and the peak and averaged slipstream at the TSI trackside and platform position. Results show that the effect on increasing nose length to reduce slipstream peak is significant in particular at trackside position. However, the influence of nose length on slipstream in tunnel is still ambiguous.

In this paper, the slipstream induced by a maglev train entering tunnel is investigated and simulated using the IDDES numerical model. This method is adopted to capture the transient turbulence characteristic and to understand the mechanism of the changing on slipstream near the tunnel portal and inside tunnel. Firstly, the grid independence validation is done to choose an appropriate mesh and the numerical model is validated by comparing the history curve of velocity and pressure with that obtained from a full-scale experiment. Then the slipstream velocity at measuring points along the tunnel is discussed in section 3.1. The magnitude and fluctuation of slipstream are analysed through the changes on instantaneous wake structure and turbulent kinetic energy (TKE) distribution. Section 3.2 further investigate the effects of nose lengths on wake slipstream and vortices inside the tunnel. The result obtained in this paper help to develop an understanding of the slipstream variations in tunnel and could present a reference on assessing transient slipstream velocity gusts in tunnels.

2. Numerical simulation

2.1 Computational method

The flow field is highly unsteady when a high-speed maglev train enters a tunnel, and the air inside the tunnel is severely compressed and its state changes over time. Considering the expression for Reynolds number: $Re = \frac{ul}{v}$, taking the train height H as feature length, which is 0.3m, the Reynolds number of the flow field around the maglev train in this study is ~2.38×10^6. This number is much higher than 2.5×10⁵, which is the critical Re for the flow around trains[31]. Therefore, overall, the solver to simulate the flow of this case is viscous, three-dimensional, compressible, unsteady and turbulent.

Some researchers solved the flow field around the train in open line using Lattice Boltzmann Method, which is mesh free and had its advantage on parallel computing[15,16,35]. Apart from this, most of researchers calculate the flow field around the train by numerically solving the N-S equations (LES, RANS). To simulate a train passing through a tunnel requires large computational resource, thus almost all studies of this problem were conducted using RANS (Reynolds-averaged Naiver-Stokes) methods. However, RANS has its shortage in that the fluctuated terms are averaged and therefore the transient characteristics of the flow and vortices cannot be observed. LES (Large-eddy simulation) is induced to simulate the instantaneous flow of train operating on open line, but the required mesh number and computational resources is still too much for simulation of moving trains. In contrast, the DES (Detached-eddy simulation) method combines the advantages of LES and RANS, to enable the transient development of large-scale vortex structures to be captured within acceptable computational resource. A drawback of this method is that the accuracy of traditional DES methods are very sensitive to grid quality and density near the wall, and may cause log-layer mismatch and grid-induced separation where the boundary layer is relatively thick and the separation region is small. As this study considers the complex interaction of the flow within changing infrastructure geometries, the IDDES model is adopted, based on the k-omega SST model to simulate the near wall region. This model has been widely adopted by previous researches to predict aerodynamic slipstream development. [2,32,34,36] The governing equation of this k-omega SST model is:

$$\frac{\partial k}{\partial t}+\frac{\partial}{\partial x_j}\left(k\bar{u}_j\right)=\frac{\partial}{\partial x_j}\left[\left(\nu+\frac{\nu_t}{\sigma_k}\right)\frac{\partial k}{\partial x_j}\right]+P_k-\beta^* k\omega \tag{1}$$

$$\frac{\partial \omega}{\partial t}+\frac{\partial}{\partial x_j}\left(\omega\bar{u}_j\right)=\frac{\partial}{\partial x_j}\left[\left(\nu+\frac{\nu_t}{\sigma_\omega}\right)\frac{\partial \omega}{\partial x_j}\right]+\alpha\frac{P_k}{\nu_t}-\beta\omega^2+2(1-F_1)\sigma_{\omega^2}\frac{1}{\omega}\frac{\partial k}{\partial x_i}\frac{\partial \omega}{\partial x_i} \tag{2}$$

$$\nu_t=\frac{a_1 k}{\max\left(a_1\omega,|\bar{s}|F_2\right)} \tag{3}$$

F_1 and F_2 represent the SST blending functions. Detail of the equations could be found in Liu, et al.[37] .In IDDES model, the sink term in equation(1) is solved as follows:

$$\beta^* k\omega \rightarrow \frac{\rho k^{3/2}}{l_{HYBRID}},\ l_{HYBRID}=\tilde{f}_d(1+f_e)l_{RANS}+(1-\tilde{f}_d)l_{LES} \tag{4}$$

l_{HYBRID} is modified length scale to combine DDES with WMLES scales. Multiple length scales are introduced in this formula, where the length scale of RANS is defined as $l_{RANS}=\kappa^{1/2}/\left(C_\mu\omega\right)$ and the length scale of LES is defined as $l_{LES}=C_{DES}\Delta_{IDDES}$. The elevating function $f_e=\max\left((f_{e1}-1),0\right)\psi f_{e2}$, aiming at preventing the excessive reduction of the RANS Reynolds stresses. The blending function $\tilde{f}_d=\max\left((1-f_{dt}),f_B\right)$ and $f_{dt}=1-\tanh\left((8r_{dt})^3\right)$where the empirical blending function $f_B=\min\left(2\exp(-9\alpha^2),1.0\right)$. By this way the length scale l_{HYBRID} is able to transfer between l_{WMLES} and $\tilde{l}_{DDES}$. Besides, in the IDDES model, the new grid length scale is calculated by the following formula:

$$\Delta_{IDDES} = \min\left(\max(0.15d, 0.15\Delta, \Delta_{min}), \Delta\right) \tag{5}$$

Where Δ_{min} is the minimum distance between the center of a grid cell and the center of an adjacent grid cell.Readers may find the complete formulations of the in IDDES model in Shur, et al.[38]. The relevant control equations are solved using the CFD software STAR-CCM+ based on the finite volume method (FVM), and a SIMPLE pressure-velocity coupling method is also adopted. The second-order upwind scheme is used for the discretization of the convection and diffusion terms. The time derivative is discretized using the second-order implicit scheme for the unsteady calculation. The time step Δt is set as $4*10^{-5}$s, estimated by CFL (Courant–Friedrichs–Lewy) $\leqslant 1$($CFL = \Delta t \cdot v/\Delta x_{min}$, where v is the train operating speed and Δx_{min} is 0.005m in this paper)[36,30].

2.2 Model and computational domain

In order to obtain the information of the viscous boundary layer and control the total number of grids at the same time, a 1:10 reduction ratio in size is used for the maglev train and tunnel model. The shape and velocity of the maglev train model selected in this paper is based on the TR08 maglev train operating in Shanghai, with two carriages of a total length of 54.4m. The size of the train and track is given in **Figure 1**(a). The width and height of the maglev train are referred as characteristic width (W) and height (H) in this paper. The original streamlined length of the train head is 5.4m and is stretched to 7.4m and 9.4m in the axial direction to study the influence of the nose length. The cross-sectional area of the single-tracked tunnel is 100m^2 and the length is 2000m.

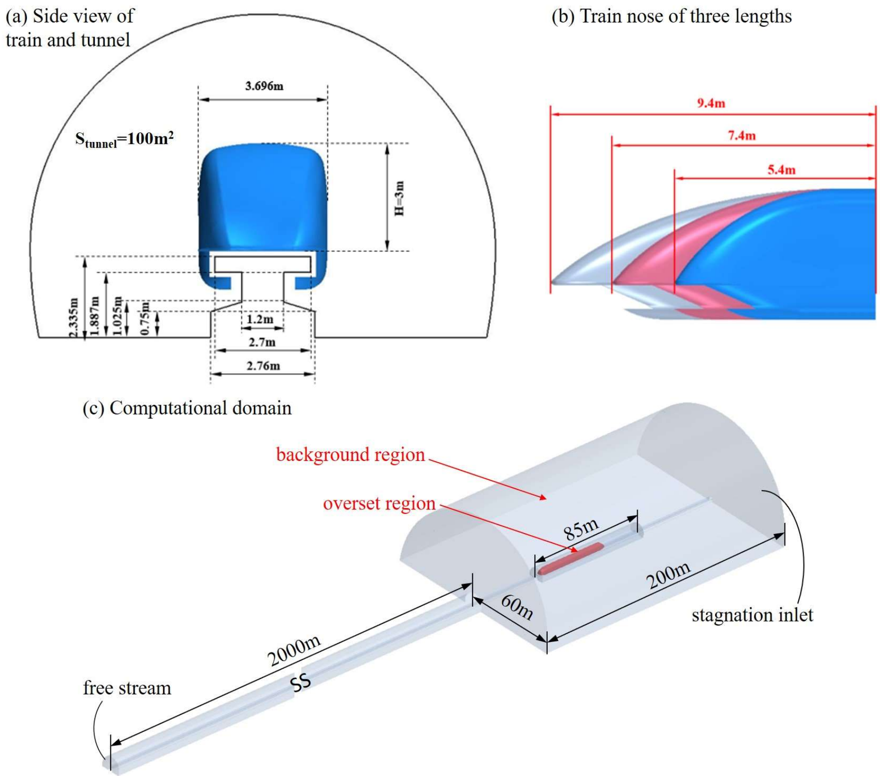

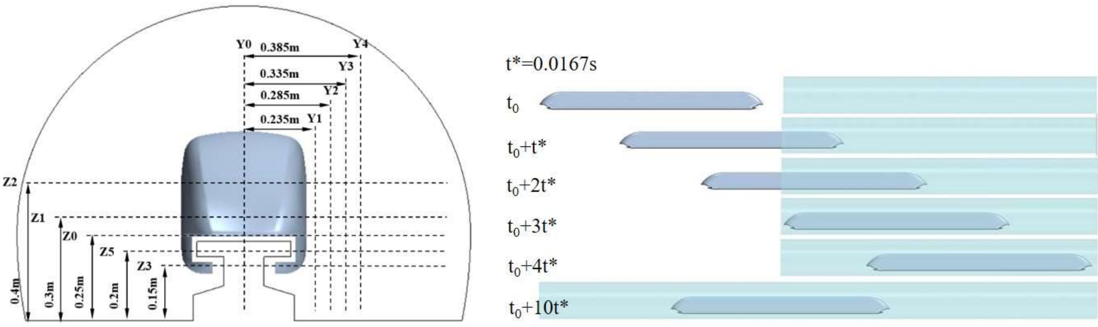

(d) positions of measured slipstream velocities (e) positions of maglev train at different moments

Figure 1 Schematic diagram of the maglev train model and computational domain

An overset mesh is adopted over sliding mesh techniques to simulate the train's motion, since the continuous development of vortices through interface have strict requirement for the accurate information transfer between stationary and moving regions. Different from the sliding mesh method that uses a uses a first-order area-based interpolation,[39] the overset mesh technique is considered as a high-order interface treatment and has been well-developed in the past decade to improve the accuracy and quality of the simulation at interface meshes[40]. The whole computational domain of maglev train entering the tunnel is divided into two regions: overset region and background region, as shown in **Figure 1**(c)(note that dimensions are given as full-scale values). The maglev train is started 50m away from the tunnel entrance to ensure that the flow field around the train is well-developed before it enters the tunnel. The train tail is 100m away from the domain boundary, which is long enough to ensure that the contribution of dissipation of turbulence vortex to the flow around the train is negligible. To avoid overlapping, such as grid interpolation errors affecting the flow field information near the train and the wake region, the cross-sectional area of the overset region is 0.9 times the cross-sectional area of the tunnel and the distance of the train tail to the boundary of overset region is approximately 10H.

The boundary settings are also given in **Figure 1**(c). For the overset region, the grids used for interpolation calculation are overset boundary, and the surfaces of the train are set as a wall. For the background region, the end of the tunnel is given a free stream boundary, the back surface of open field is set as stagnation inlet, and the rest are set as wall. The distribution of measuring points of slipstream velocities is shown **Figure 1** (d). Besides, different time instants of the maglev train entering the tunnel are chosen as shown in **Figure 1** (e) to analyse the change of slipstream and vortices, where t* is the time required for the maglev train to travel 2m.

2.3 Mesh

The entire computational domain is divided by a trimmed cell mesh. Due to the fact that areas in which flow separation and vorticity are usually generated in are mainly located at the head/ tail of the train and the gap between the train and the track, a finer mesh is adopted in these regions. Coarse, medium and fine meshes were built to verify the independence of the grid, as shown in **Figure 2**(a). The sizes of the first cells on the train surface are 0.007m, 0.005m and 0.004m, and 15, 25 and 30 prism layers are established on train surface with at total grid number of 17.6, 27.2 and 31.7 million for the coarse, medium and fine meshes, respectively. The comparison of results from each mesh density for slipstream velocity at tunnel entrance is shown in **Figure 2**(c). It can be seen that the results agree well with each other, while the coarse mesh tends to overpredict the velocity, particularly at the wake. The peak and profile of the slipstream predicted by medium mesh is very similar to that of the fine mesh, but there is some discrepancy in the wake region. It is understandable since there are a large number of vortices exist in wake region that could be captured using IDDES method, the flow there is highly unsteady and the velocity variation is related to both space and time. Therefore, it is inevitable that the transient velocity curve in the wake region cannot be the same at a specific moment and position. Similar conclusion could be seen in mesh validation in Khayrullina, et al.[30], in which utilises the LES method to simulate a train passing through a platform, and the velocity profile at wake region also deviates a lot between fine and medium mesh. Thus, medium mesh is adopted in this paper.

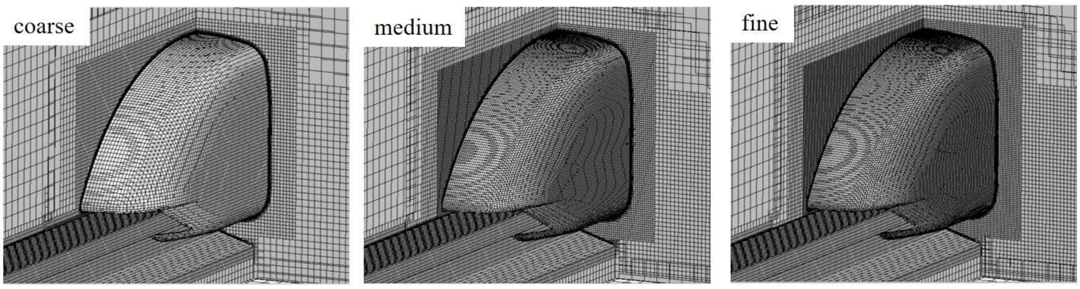

(a) three set of mesh

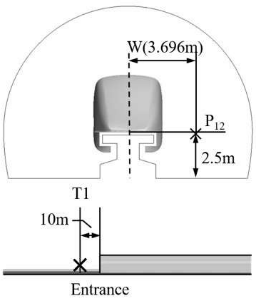

(b) position of measuring point

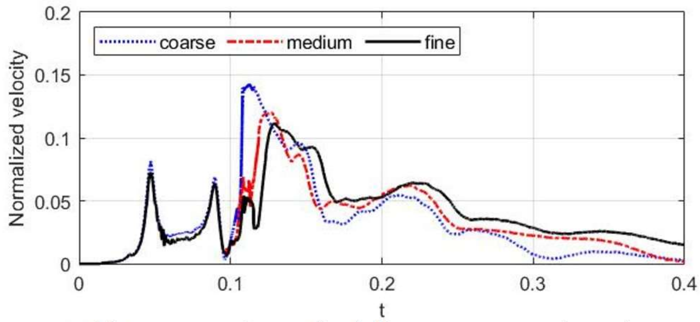

(c) history curve of normalized slipstream at measuring point

Figure 2 Result of mesh sensitivity

The specific diagram of the mesh at tunnel entrance, around train and track is shown in **Figure 3**(b). In order to better simulate the velocity distribution in the viscous flow region of the train, the first layer of the wall is estimated with a thickness of y+ ≈ 5, with 25 prism layers and a stretching ratio of 1.15. A coarser prism mesh is added on tunnel and track surface. The wall y+ of train surface at 10t* after the train entered the tunnel, as shown in **Figure 3**. It can be seen that y+ for most of the mesh on train body is less than 3. To ensure high interpolation accuracy for overlapping grids and successful mesh assembly during train motion, the size of the acceptor cells in the overset region is similar to that of the donor cells in the background region. There are 0.02 m and 0.032 m for the acceptor and donor cells, respectively. The mesh for the overset and background region are coloured with blue and black in, with corresponding grid numbers of 16 and 11 million, respectively.

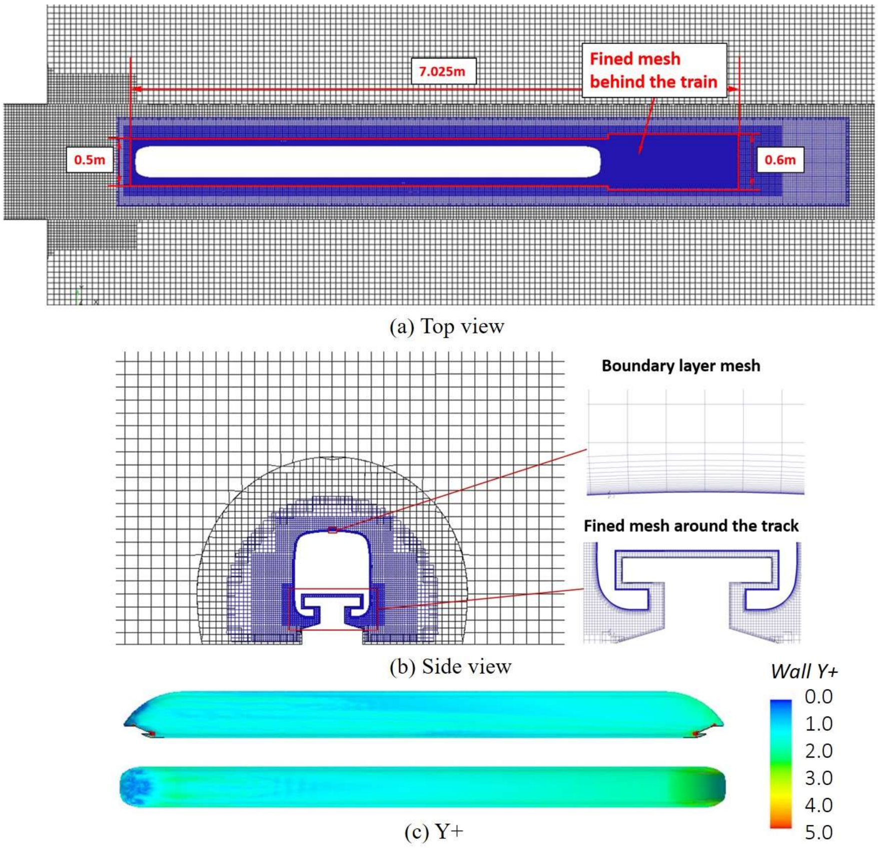

Figure 3 Computational mesh

2.4 Model verification

In order to verify the accuracy and the reliability of the numerical setup in this paper, the numerical simulation results of a CRH2C train passing through a tunnel at a speed of 300km/h are compared with the results obtained from a full-scale experiment. The test train is composed by eight cars with a total length of 201.4m and a running speed of 300km/h. The tunnel is a double-track tunnel with a total length of 1005m and a cross-sectional area of 100m^2. Besides, a buffer structure with pressure relief hole is constructed at tunnel entrance and exit. More details of the pressure and velocity monitor sensors and the setup of full-scale experiment are illustrated in Liu et al (2019) [25].

Based on the train and tunnel model of the full-scale experiment, the dimensions of the computational domain for the validation case is constructed as shown in **Figure** 4. A 1:10 reduction ratio in size is used for the CRH2C train and tunnel, which is the same as the reduction ratio for the maglev train in this paper. Similarly, the boundary conditions and the cross-sectional shape of the overset region are also determined following the setup adopted for the maglev train in this paper.

A trimmed cell mesh is adopted to divide the overset and background region as shown in **Figure 5**. Mesh around the train nose, the wake region and tunnel portal are refined with a size of 0.00625, which is a bit coarser comparing to the grid size adopted for the maglev train in this paper. This is due to the test train is composed by 8 cars, which will generate massive grid number if completely follow the grid size in this paper, leading to extremely high computational costs by using IDDES numerical model. The first layer of the wall is estimated by y+≈5 with a thickness of 0.01, with 13 prism layers and a stretching ratio of 1.5. The size of the acceptor cells in the overset region and the donor cells in the background region are both 0.025m. By this way, the total grid number for overset region and background region are 11.2 and 14.7 million respectively.

The slipstream and pressure history curve obtained from the simulation are compared with that from the full-scale experiment as shown in **Figure 6**. Due to the reduced scale of the simulation, time and pressure are non-dimensioned by L_{tr}/v_{train} and $0.5*\rho*v_{train}^2$ respectively for a better comparison. It could be seen in **Figure 6**(a) that in general the simulation result fits well with the experimental result on predicting the velocity peak induced by train nose and near wake region, with a relative error of 3.5% and 6.4%. However, the velocity distribution in the wake region doesn't match in a very good way, which is understandable since the instantaneous velocity obtained from one run is unsteady due to the highly turbulent flow, especially in the wake region. Besides, the velocity around the train body is a little underestimated by the simulation, this might due to the reduced-scale and the simplification on bogies potentially decreasing the effective blockage ratio. Overall, the prediction on the peak values and trend of the velocity are within acceptable error range. **Figure 6**(b) shows the comparison of pressure coefficient on tunnel surface. The maximum positive and negative pressure coefficient obtained from the simulation are 0.3449 and -0.5633, and that from the experiment are 0.3505 and -0.5759, respectively. Therefore the relative error for the peak-to-peak pressure coefficient of tunnel train surface does not exceed 2%. The deviation between the simulation and full scale test at the second half section of time history curve of pressure on tunnel surface might due to the effect of environmental wind and certain error of actual running velocity during the experiment. In conclusion, the magnitude of slipstream and pressure wave could be satisfactorily predicted using the simulation settings in this paper.

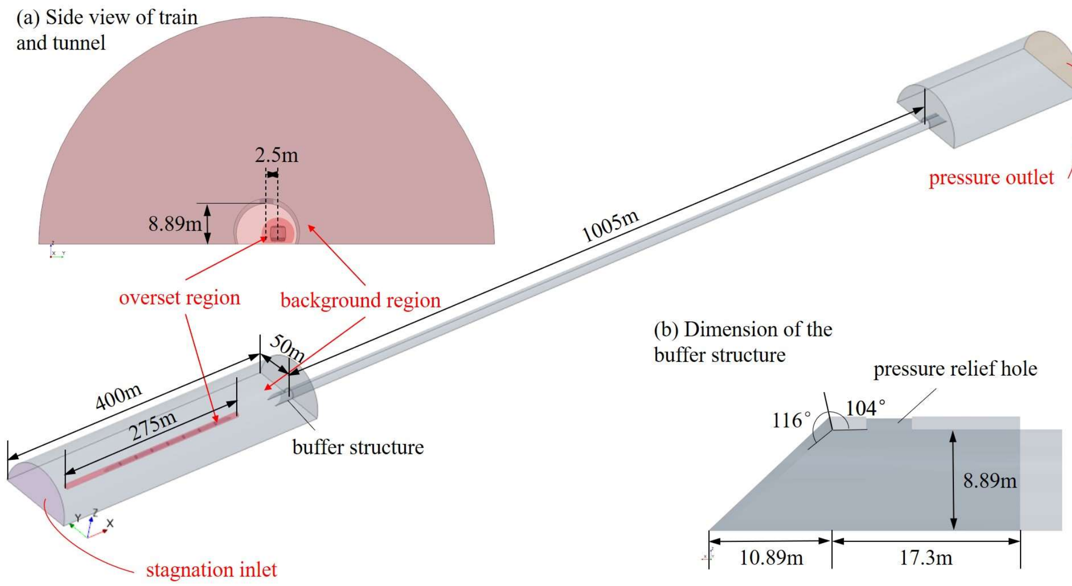

Figure 4 Computational domain for the validation case

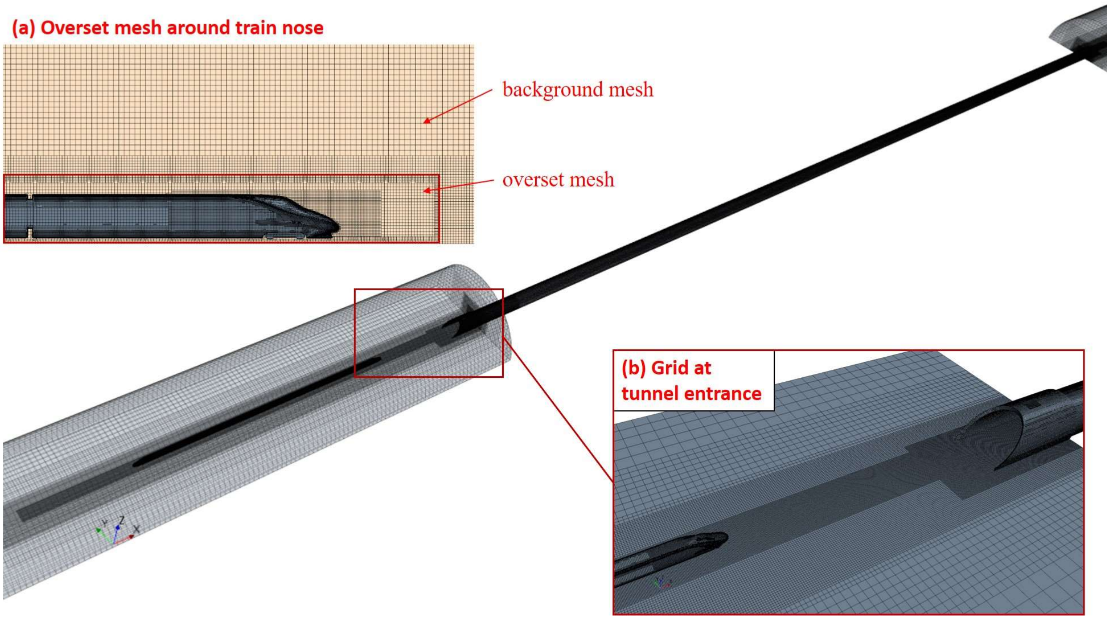

Figure 5 Computational mesh for validation case

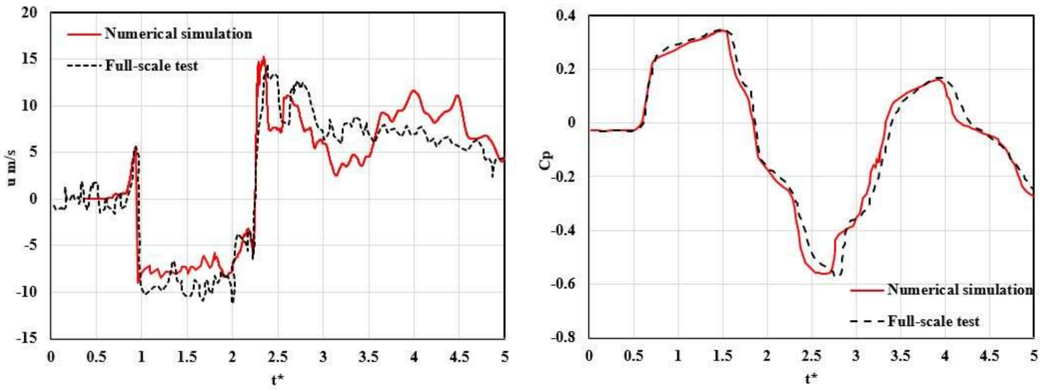

(a) (b)

Figure 6 Comparison of full-scale test and numerical results (a) velocity variations (b) pressure variations

3 Numerical results

3.1 Reference case

3.1.1 Slipstream velocity

As referred to in the TSI and EN, horizontal velocity plays the vital role in the safety risk of instability for trackside workers and lineside equipment. Throughout this analysis the slipstream velocity is therefore defined by the horizontal velocity, and normalized by the train speed as below,

$$\mathrm{U} = \frac{\sqrt{u^2+v^2}}{v_{train}} \tag{1}$$

where u and v represent the streamwise and spanwise direction of the flow velocity, v_{train} is 119.4m/s. The history curves of the normalized slipstream velocity at positions T1~T7 are shown in **Figure** 7 (b)~(h), measured for 3 points at each position (P_{11}, P_{12}, P_{13}). The position of the 21 measuring points relative to the train and tunnel is shown in **Figure 7**(a). The red and blue dashed lines represents the nose and tail of the train, and red and blue arrow represents the compression wave and expansion wave, generated when train head and tail enters the tunnel separately.

The profile of slipstream at measuring points inside tunnel is affected by both the expansion and compression pressure waves and the passing train. The influence of the pressure waves could be concluded, from **Figure 7**(d)~(e), to increase slipstream velocity magnitudes where the compression wave passes and decrease the slipstream magnitude when the compression wave passes. The influence of the passing train on the slipstream in tunnel is analysed based on the flow regions proposed in Baker[7,41,42]: nose region around the front of the train, boundary-layer region along the length of train, wake region (near-wake and far-wake region) behind the train. For measuring position P_{12}, the height at which is the same as the track upper surface, the slipstream shows a significantly larger wake velocity among P_{11}~P_{13}. At T1 outside the tunnel entrance, a peak occurs at nose region and tail of boundary region, with a more significant peak is observed at “near wake region”. This is consistent with findings from previous research for a train running on the open line. When the train passes T2, the slipstream velocity at “boundary layer region” and “near wake region” increases due to the piston effect. As the distance from the measurement point to the tunnel entrance increases (from T3 to T5), the velocity at nose and boundary regions gradually increases, while the peak at the wake increases to its maximum at T4 then decreases. To be more specific, the velocity at the rear of boundary layer region reaches the maximum soon after it enters the tunnel, then the velocity at the body and head of boundary layer region reaches the maximum gradually, at approximately 100m inside the tunnel. The profile and maximum peak magnitude of slipstream in each region at measuring points T5, T6 and T7 shows slight difference. This could be due to the position of the measurement points far from the tunnel entrance, therefore the velocity of the wake is almost no longer affected by the train entering the tunnel.

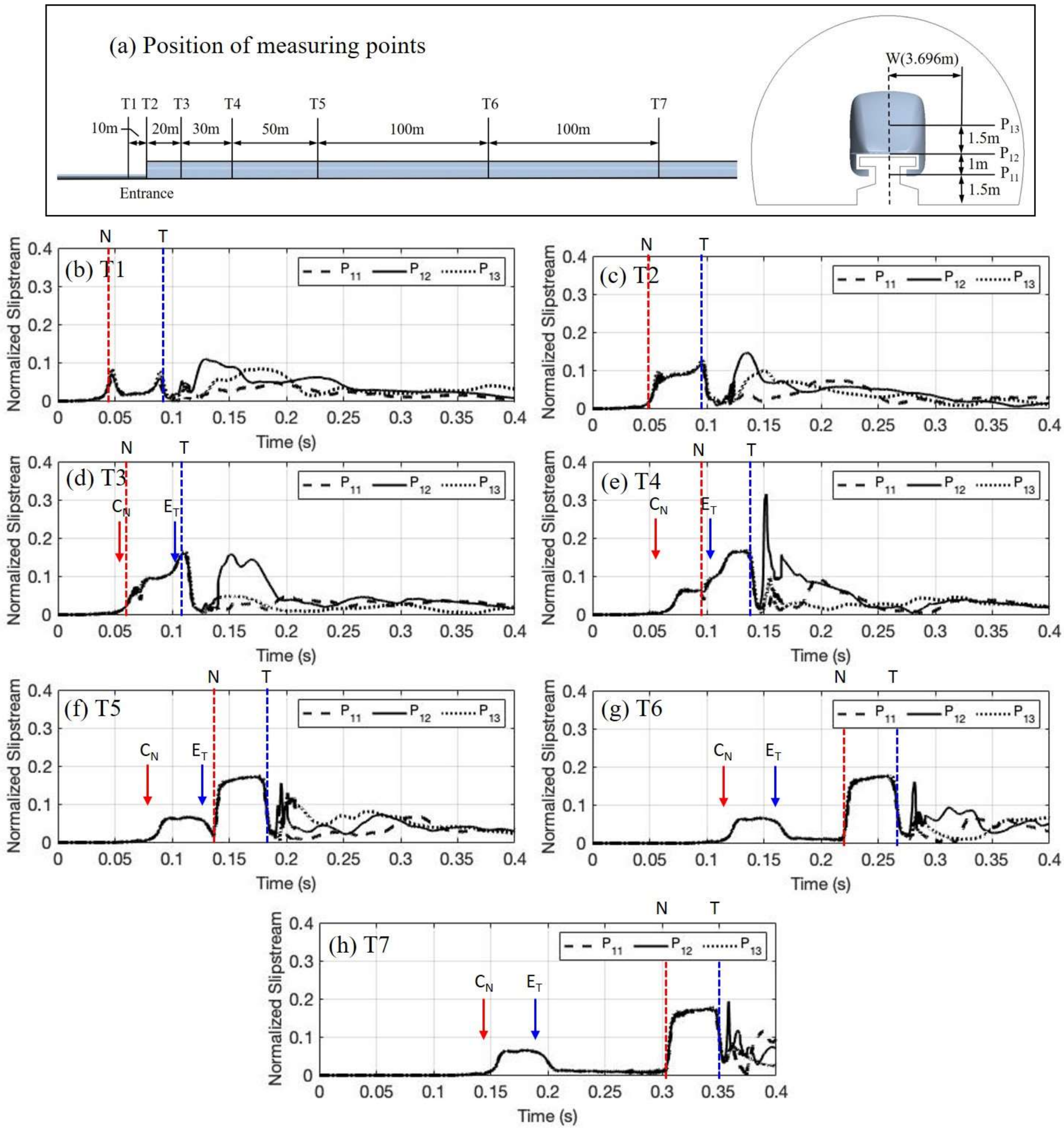

Figure 7 Time history curve of slipstream velocity

3.1.2 Wake vortex structure

Slipstream velocity is closely related to the distribution and strength of wake vortex. To understand the change of velocity as the train enters into the tunnel, the instantaneous vortices generated around the maglev train, identified by Q iso-surface, are shown in **Figure 8**. The contours of the particle movements at X1=1/3H and X2=3H are given to analyse the development of the instantaneous vortices.

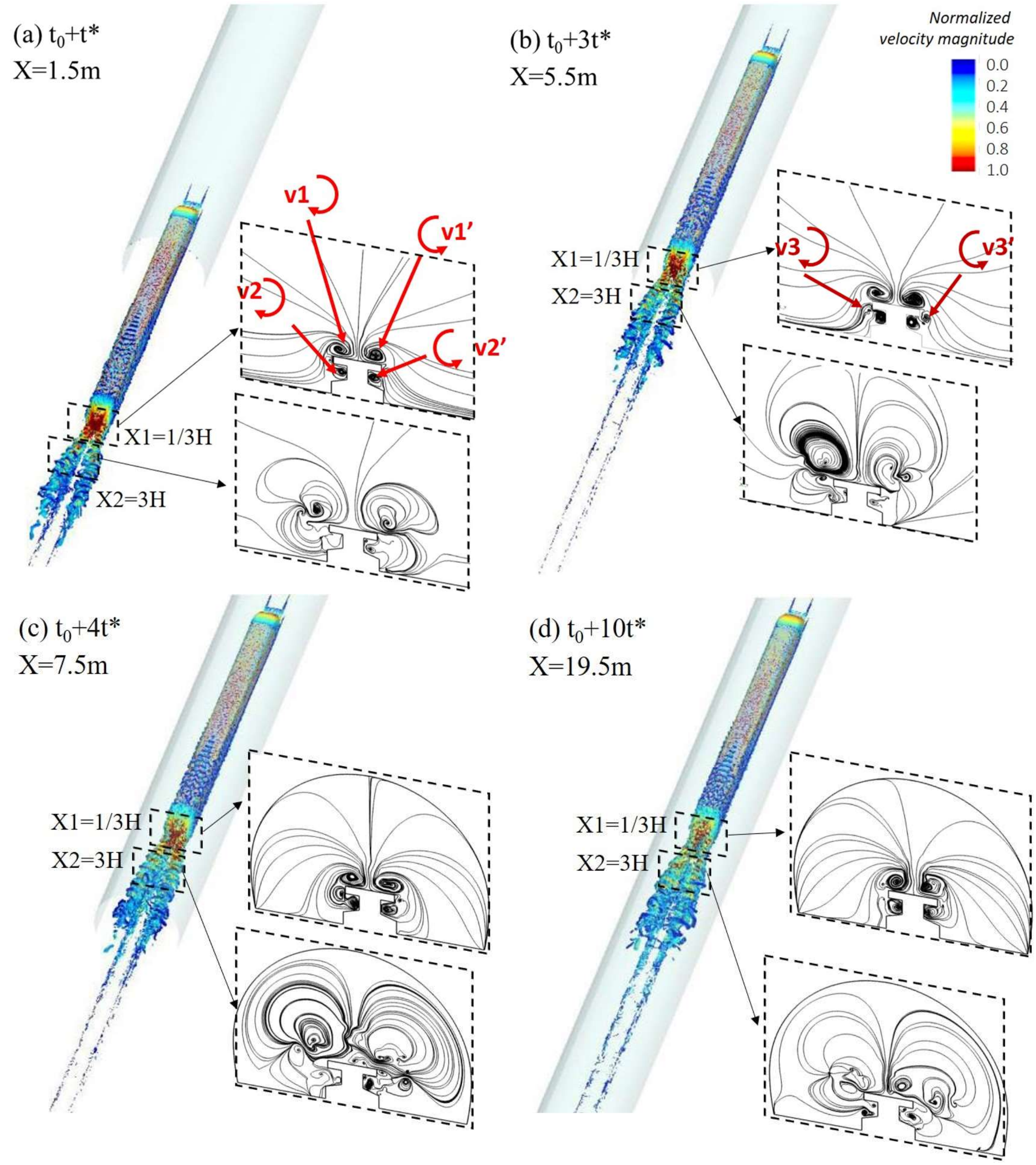

Figure 8 Q iso-surface at different moments of maglev train enters the tunnel（Q=100000）(X: the distance from the head of the train to tunnel entrance)

As the air accelerates and flows downward at the tail of the train, the backpressure gradient and the momentum loss in the boundary layer increases. It forces the boundary layer to separate, forming a pair of large-scale symmetrical vortices (v1 and v1'), which can be seen clearly in **Figure 8**(a) when the train tail is far away from the tunnel entrance. This pair of coherent structures is the most significant one in the wake region of a maglev train, and its formation mechanism is similar to that of a high-speed train. Since the track of a maglev train is different from that of the high-speed train, there is another pair of smaller vortices (v2 and v2') beneath the maglev track. Besides, this two pair of vortices show good symmetry with a clear shape when they just formed at contour X1= 1/3H behind the train tail due to the simple geometry of the maglev train. It is worth pointing out that normally the instantaneous flow field at near wake region of a high-speed train is much more dis-ordered since the bogies and windshield generate large amount of turbulence that finally goes into the wake [2,8,34]. The vortices generated by the maglev train gradually develops as the distance from the rear of the increases. At the contour father from the tail of the train (X=3H), these pair of large-scale vortices split into weaker and small-scale coherent structures. Besides, the velocity in the near wake region decreases with the vortices shedding backwards, and the velocity magnitude near the vortex core is larger than that at the outer edge of the vortex. At t_0+3t*, the rear of the train has just entered the tunnel entrance. Due to the blockage effect, the velocity sweeping downwards at the rear of the train increases, leading to a spanwise moving tendency of the vortex structure close to the rear of train. Also, a small pair of vortices (v3 and v3') formed as the air flow over the side of train surface and interact with the side of the upper track, which could be seen at contour X1= 1/3H. The small-scale vortex v3 will split as it develops, with part of it involving in the large-scale vortices v1, and the rest spreading downward and spanwise. At t_0+4t* when the train tail is about 2m inside tunnel, the distribution of the vortex is significantly wider and the vortex length scale enlarges. The wake structure becomes disordered at the tunnel entrance due to the turbulent airflow. However, the size of tail vortex continues to grow inside the tunnel as it is shedding backwards towards the entrance, thus increasing the length of the development, as could be seen when the train head is 19.5m inside tunnel at t_0+10t*. Compared the contour at X=3H with that in **Figure 8**(a), it could be clearly seen that many small vortices generate and the air flow at the wake is more disordered when the wake is inside tunnel. The scale of the vortex inside the tunnel significantly enlarges and the distance between the two vortices narrows. Due to the acceleration of the air flow inside tunnel, an earlier separation occurs at the rear of the train so that the position where the vortex fall off moves upward, which could be seen by comparing the position of the vortex at contour X=1/3H in **Figure 8**(a) and (d). Besides, due to the larger negative pressure in the wake region, the suction effect on the wake vortices is enhanced so that the distance between the pair of vortices is narrowed. The spatial scale of the vortices in the tunnel significantly increases with the increasing velocity sweeping downward, which also explains why a relatively larger wake velocity exists on the trackside inside the tunnel.

3.1.3 Turbulence intensity

TKE is a quantity to measure turbulence quantitively, and has been used to analyse the wake of wind turbines, buildings and trains under crosswind (Influence of atmospheric stability on wind-turbine wakes: A large-eddy simulation study, 2015; Atmospheric turbulence effects on wind-turbine wakes: An LES stud, 2012; Numerical calculation of the slipstream generated by a CRH2 high-speed train, 2016; Dynamic analysis of the effect of nose length on train aerodynamic performance, 2019). In this paper, turbulent kinetic energy (TKE) is introduced to measure the fluctuation and the overall level of turbulence in the wake. It is calculated by summing the squared fluctuating velocity of the three axial directions,

$$\mathrm{TKE} = \frac{1}{2}\left(\overline{u'^2} + \overline{v'^2} + \overline{w'^2}\right) \quad (2)$$

u', v' and w' are fluctuating velocities on x, y, z direction, which are the difference between the instantaneous velocity and the average velocity. The instantaneous and average velocity adopted are monitored from t_0+5t^* to t_0+20t^*. **Figure 9**(a)(b) compares the TKE distribution in near wake region when maglev train runs on open field and inside the tunnel. The positions of the contours are 1H, 2H, 3H, 5H from the tail of the train respectively and the area of the white dashed-line square is $1m^2$.

TKE is mainly generated above and on both sides of the maglev track, where the wake vortices distribute. Therefore, it also reflects clearly the change in the scale of the vortex and the trace of the vortex shedding spanwise and upwards. The magnitude of TKE increases near the tail of the train, and gradually decreases as the distance increases. When the maglev train operates inside the tunnel, the distribution range and the magnitude is significantly larger. This is due to the larger streamwise velocity inside tunnel and the interaction of the airflow and the track, which causes a stronger velocity fluctuation in the wake. The increase in distribution range is consistent with the conclusion that the spatial scale of the wake vortex in the tunnel is larger than that on the open line. It is worth noting that the distribution of the vortex inside tunnel ranges mainly between 2m~4m above the ground, and 0.5m~3.5m from the centre of the train (COT). It explains the relatively low velocity peak in the wake at measuring points at Y=0.3696m (section 3.1.1).

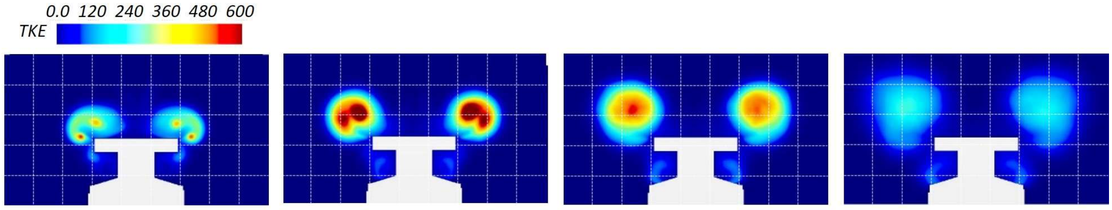

(a) TKE distribution on open field (X/H=1,2,3,5)

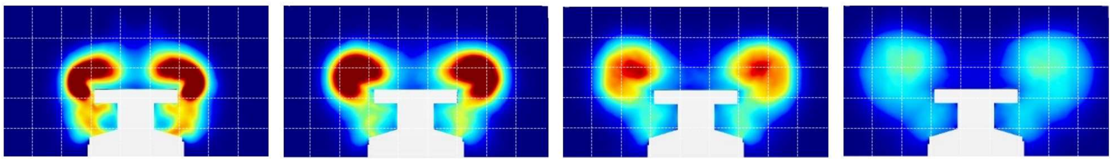

(b) TKE distribution inside tunnel (X/H=1,2,3,5)

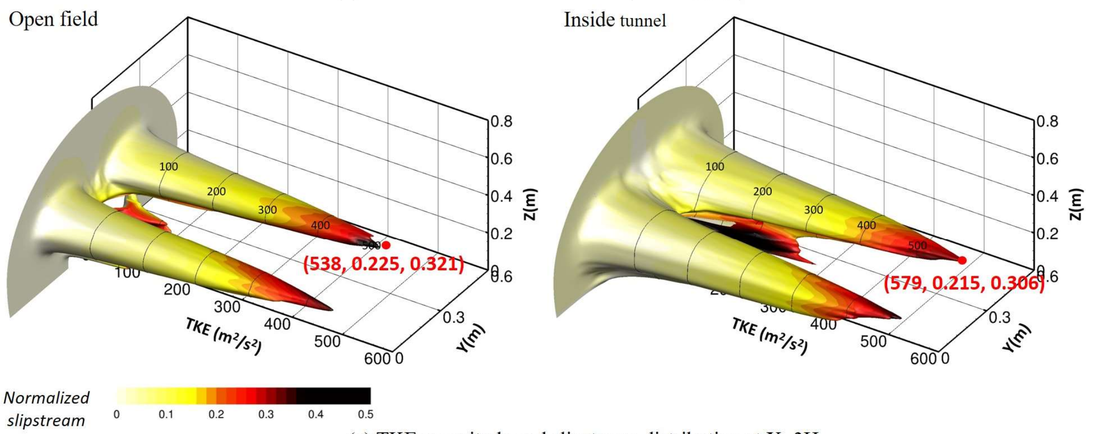

(c) TKE magnitude and slipstream distribution at X=3H

Figure 9 Distribution of TKE at contours behind the train (X/H=1,2,3,5)

To quantitively compare the TKE generation before and after maglev train entering the tunnel, the magnitude of TKE at contour X=3H is shown in **Figure 9**(c), and is coloured by normalized slipstream. The maximum slipstream near vortex v1 doesn't show much difference, however the maximum velocity and TKE near vortex v2 is much larger inside tunnel. The position and magnitude where maximum TKE generates are marked in the figure. It could be seen that at this contour, the maximum TKE generated inside tunnel is. 7.62% larger than that on the open line. Besides, both y and z coordinates inside tunnel are smaller than those on the open line. It indicates that the flow development of wake vortex is constrained by the tunnel wall, leading to the position of vortex core slightly closer to the track and COT.

3.2 The effect of nose length

3.2.1 Slipstream velocity

As we discussed in 3.1.2, the maximum slipstream velocity is expected to occur from Z=0.2 to Z=0.3 where the main wake vortices generate. Therefore, the measuring points are located at Z=0.2, 0.25, 0.3 and 0.4 m to try to capture the maximum slipstream velocity when y (the distance from measuring point to central line) is constant. The spatial distribution of normalized slipstream along the streamwise direction of the maglev train before and after train tail enters the tunnel (t_0+t* and t_0+10t*) is shown as **Figure 10**. The position of the measuring points relative to the train and the location of the train at different time are shown in **Figure 1**(d)(e) respectively. The range of x-axis of the measuring lines are from 1m ahead the train nose to 6m behind the train tail. The two vertical dash lines in **Figure 10** represent the position of train head and tail, and the bold line is the position of the tunnel entrance. The peak value and the position where it appears are marked red in the figure.

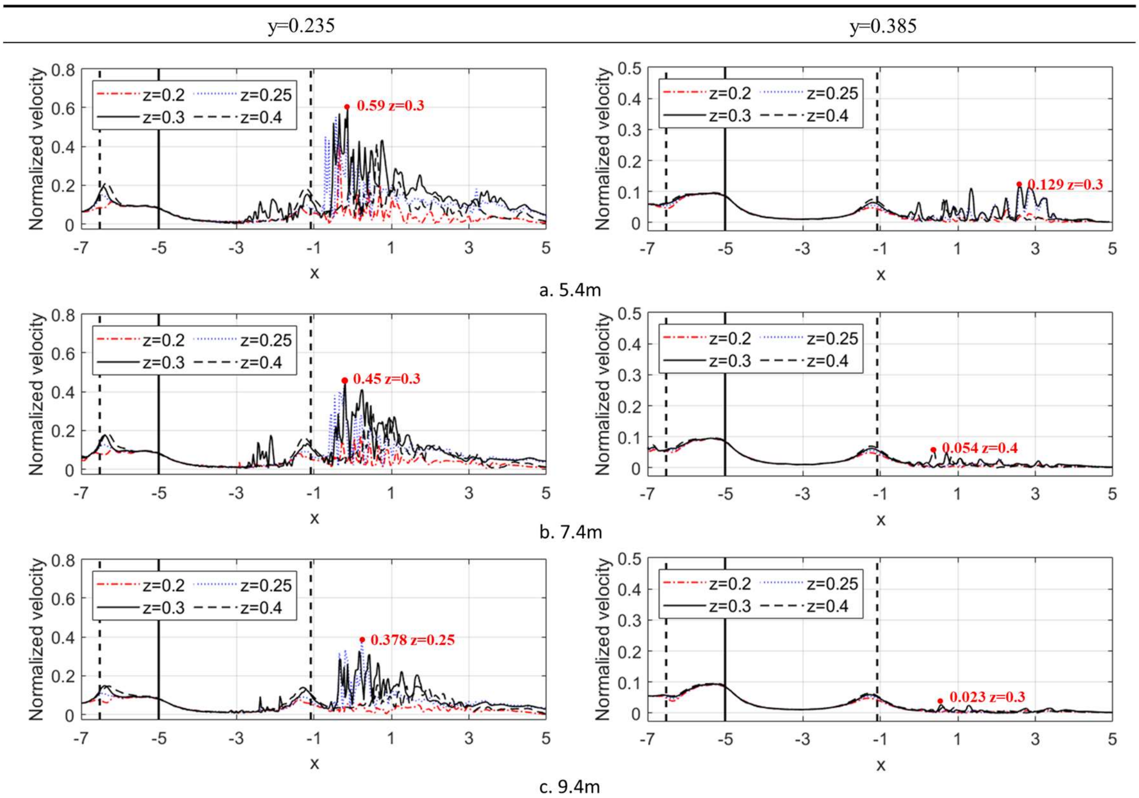

(a)

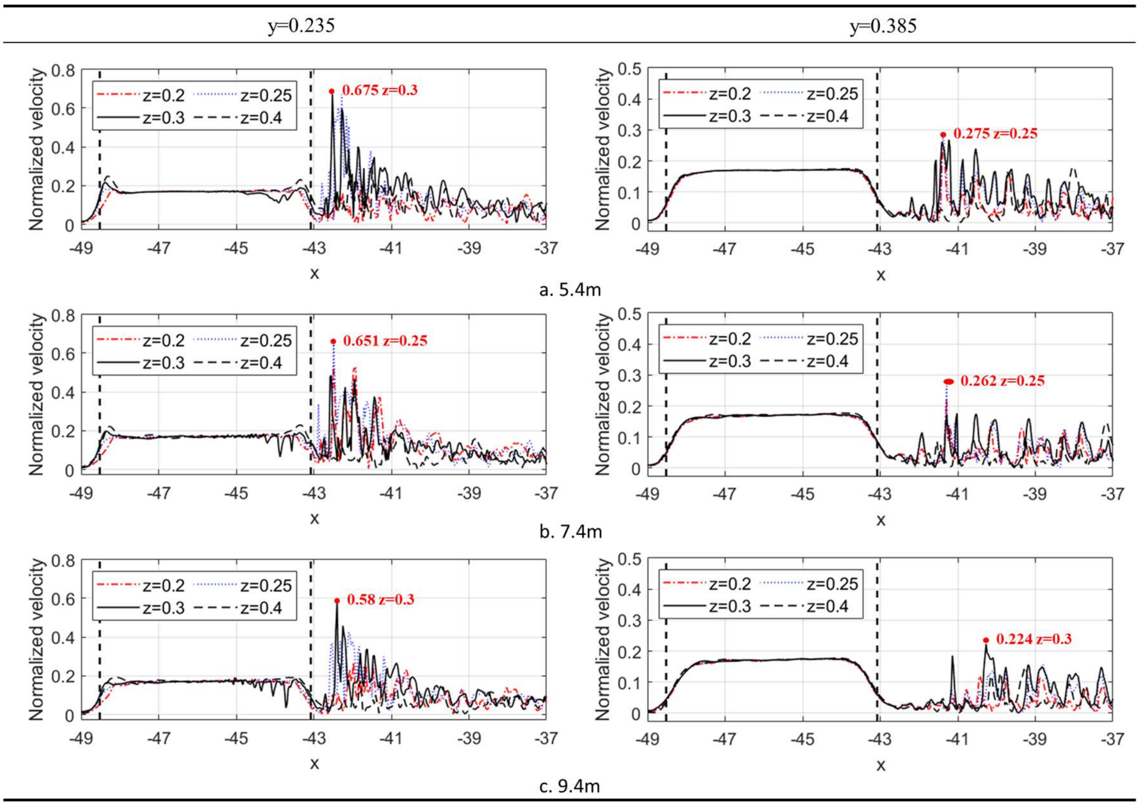

(b)

Figure 10 Spatial distribution of normalized slipstream for maglev trains of three nose lengths at different positions (a) t_0+ t* before the train tail enters the tunnel (b) t_0+ 10t* after the train tail enters the tunnel

The maximum slipstream velocity occurs at 0.25m~0.3m above the ground for maglev train of three nose lengths. After the maglev train enters the tunnel, relatively larger wake slipstream and fluctuation amplitude still exists at the position 20*H* from the rear of the train and 0.96*W* from COT. The slipstream in the annulus space between the train body and tunnel is basically unchanged when the nose length increases from 5.4m to 9.4m, but the reduction of the peak of the wake slipstream velocity and the reduce rate on its lateral and vertical direction is significant. Before the maglev train enters the tunnel, the peak of wake slipstream of the maglev trains with nose lengths of 7.4m and 9.4m is reduced by approximately 23.7%(58%) and 35.9%(82.2%) at 0.235m(0.385) from COT, compared to that of maglev with nose length of 5.4m. When the train is operating in the tunnel at t+10t*, the increase of wake slipstream of the maglev train with a longer nose length is more notable. The peak of the wake slipstream of the maglev trains with the 7.4m and 9.4m nose lengths at Y = 0.235m(0.385) is reduced by about 3.6%(4.7%) and 14%(18.5%), respectively. It can be concluded that the effect of increasing the nose length to reduce the wake slipstream peak velocity magnitudes is weakened inside the tunnel. To understand the difference on slipstream between three nose lengths, the flow pattern and wake structure are further analysed in the following sections.

3.2.2 Wake vortices structure

Figure 11 considers the influence of the nose length on the wake vortex structure when the maglev train operates on open line and inside tunnel. The vortices are identified by Q criteria and coloured with vorticity.

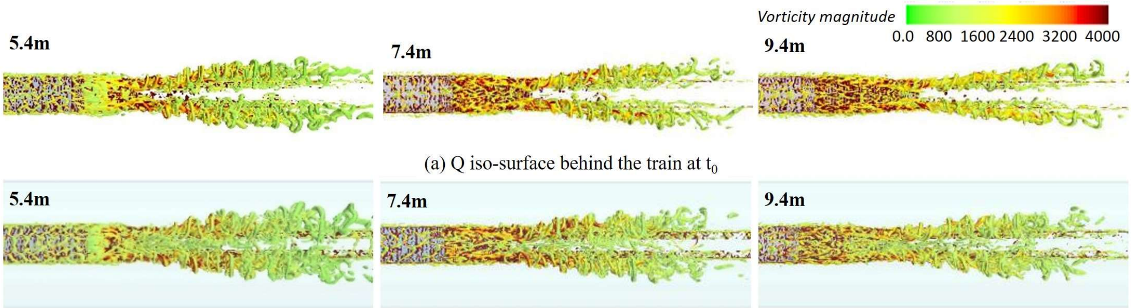

(a) Q iso-surface behind the train at t_0

(b) Q iso-surface behind the train at t0+10t*

Figure 11 Q iso-surface at the wake of maglev train with different nose lengths（Q=100000）

The pair of large scale vortices induced by the separation at train tail are clearly identified in **Figure 11**. Comparing the vortex structure on open line to that inside the tunnel, it could be seen the wake of the train with three different nose lengths exhibits a similar behaviour, that is, the vortices are notably wider along with much more small-scale vortices generated when inside the tunnel. This is due to the relative speed between the train and the surrounding air increases inside the tunnel, and the mixing effect created by the confined space is strengthened. Besides, The tail of the train is covered by high vorticity, indicating a strong circulation region. Vorticity is higher where closer to the core of the vortex, and gradually weakens as the wake vortices shedding spanwise and backwards. As the nose becomes longer, the scale of separation for the pair of vortices at the rear of the train is thinner and the angle between the vortices becomes narrower. It is hypothesised that this is due to the longer train nose decreasing the negative pressure behind the train tail, reducing the suction and delaying the separation at the tail of the train. Besides since the velocity peak exists where close to the core of vortexes, the thinner and narrower vortices generated by longer train nose explains the smaller slipstream. Comparing to **Figure 11**(a) and (b), this phenomenon is more significant before the train enters the tunnel, which explains why the effect of nose length on reducing wake velocity is less obvious inside tunnel. The small-scale vortices generated by the maglev train entering the tunnel become less with increased nose length, and the vortex complexity is therefore reduced. The magnitude of TKE in the wake is given in the next chapter to quantitively compare the wake unsteadiness inside the tunnel induced by different nose length.

3.2.3 Turbulence intensity

In order to measure the influence of nose length on the fluctuation of the wake inside tunnel, the magnitude of TKE of different nose length inside tunnel at contours X=2H/3H/5H behind the train are shown in **Figure 12**. The detail of how TKE in tunnel is calculated and averaged is illustrated in 3.1.3.

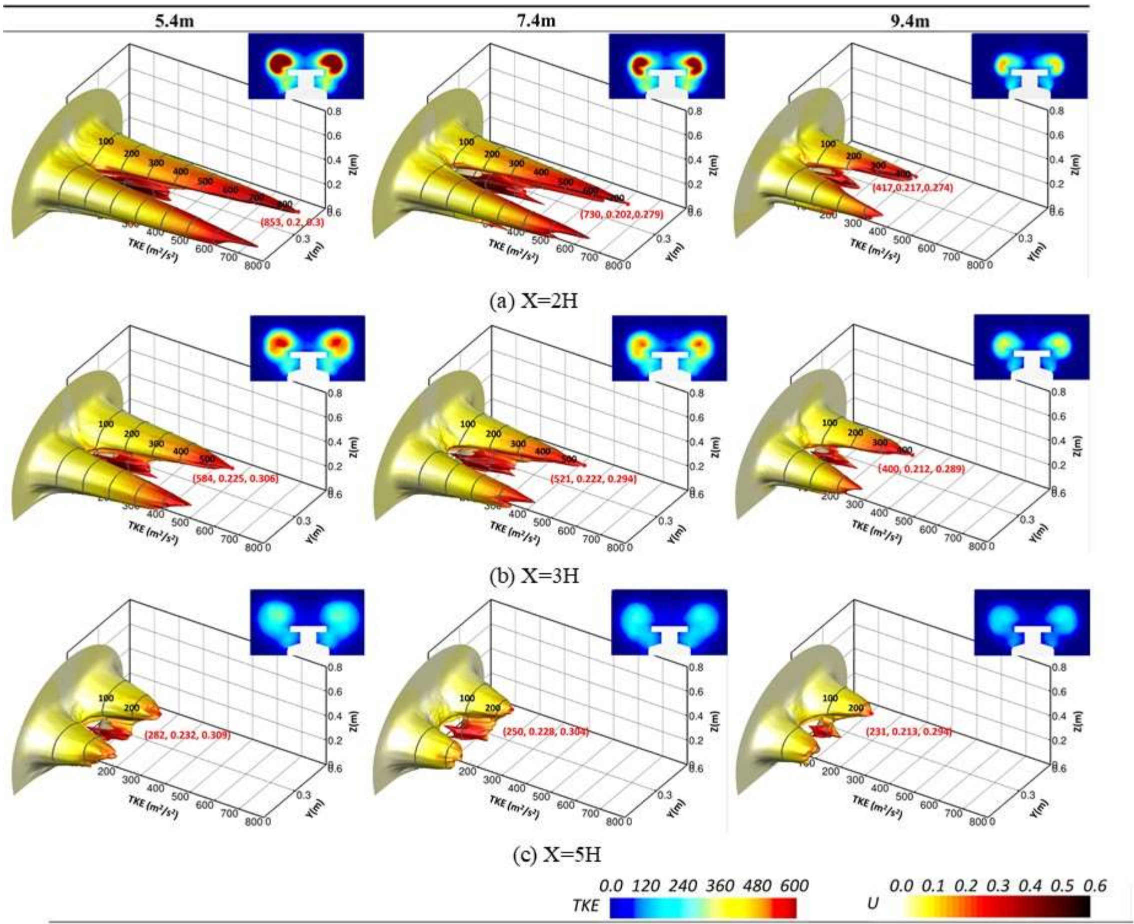

Figure 12 TKE and slipstream distribution of different nose length inside tunnel at contours behind the train (X/H=2,3,5)

As the distance from the train tail increases, the main TKE distribution area moves upward and sideward as the vertical movement and extension of the wake vortices. The magnitude and distribution area of TKE significantly decreases as the length of the train nose increases, and this phenomenon is particularly obvious in regions closer to train tail and for the case with nose length of 9.4m. This phenomenon is mainly related to the longer train nose delaying the separation of the boundary layer at the rear of the train, which leads to a significant reduction in the speed fluctuation in the three directions, further result in the reduction of the TKE. Comparing to that of 5.4m, the maximum TKE at contour X=2H/3H/5H decreases about 14.4%/10.7%/11.3% and 51%/31.5%/18% as the nose length increase to 7.4m and 9.4m respectively. It illustrates quantitively the reduction of the fluctuation of slipstream velocity with the increase in nose length, and is consistent with the conclusion that vortex structures are thinner as nose length increases. The magnitude y and z axis where the maximum TKE generates inside tunnel is marked in the figure, also indicating how the position of the vortex core changes with the length of train nose. Considering the height of the track is 0.2335m , it could be seen that comparing to the that of 5.4m, the magnitude of where the maximum TKE generates above the track at X=2H decreases about 31.6%/39% as the nose length increases to 7.4m/9.4m. It is also noticed that the location of vortex core is closer to COT at contour X=2H when the train nose is shorter, and farther from the COT as the vortices developing away from the tail of the train(contour X=3H/5H). This might due to the larger negative pressure region generated by the shorter train nose at the rear of the train suctioning the flow to the COT. In the meantime the scale of the pair of counter-rotating vortices generated by shorter train nose is larger, and therefore moves further away from each other in spanwise direction as they shedding backwards. In general, the location is about 0.5~0.7 m above the track and 2.1~2.2 m to the COT, which matches the area where the peak of slipstream exists. However, though the area where high slipstream distributes significantly decreases with the increase of nose length, the maximum slipstream doesn't show much difference among three nose length.

4 Conclusion

Due to the special track structure of the maglev train and its simplification on bogies compared to high speed train, the slipstream variation and development of wake vortex structure are different from that generated by high speed trains. For the first time the process of a maglev train entering a tunnel is simulated using the overset mesh method through an IDDES numerical simulation. The vortex structures and TKE distributions change as the maglev train operates from open line to a tunnel are discussed in detail, combining with its relationship with the magnitude and fluctuation of the slipstream velocity. Besides, an approach to calculate the TKE inside tunnel is proposed, enabling to quantitively analyse and compare the effect of confined space on the fluctuation of slipstream and the turbulence level of the wake. The effect of three nose lengths are further investigated. A series of important conclusions can be drawn as follows:

(a) The magnitude and fluctuation of the slipstream inside tunnel are significantly higher than that in open line. As the distance of measured points closed to the tunnel entrance increases, the slipstream velocity at the rear of boundary region and wake region increases first, then the velocity at the head of boundary region increases gradually. As the distance further increases, the slipstream at "boundary layer region" keeps constant at its maximum, while that at the "near wake region" decreases slightly then remains basically unchanged.

(b) As the train enters the tunnel, the velocity sweeping downwards at the rear of the train increases, leading to a spanwise moving tendency of the vortex structure close to the rear of train. The spatial scale of the tail vortex increases significantly and the distance between the vortices becomes wider, explaining the larger velocity exits inside tunnel at the same position relative to the train.

(c) The magnitude of TKE near the train tail increases rapidly then gradually decreases as the distance to train tail becomes longer. When operating inside a tunnel, the maximum TKE at X=3H is. 7.62% larger than that on the open line, indicating the larger velocity fluctuation inside tunnel.

(d) With increasing nose length, the spatial scale and complexity of the tail vortices decreases, and the distance between the two flow direction vortices becomes narrower. This effect is more obvious when compared to results from an open line. Comparing to the nose length of 5.4m, the z position (above the track) of vortex core inside the tunnel at contour X=2H decreases about 31.6%/39% as the nose length increases to 7.4m/9.4m.

(e)The location where the maximum TKE is generated is similar among the three noses, which is about 0.5~0.7 m above the track and 2.1~2.2 m to the COT, but the value and distribution area of TKE inside tunnel are both significantly reduced. Comparing to that of 5.4m, the maximum TKE at contour X=2H/3H/5H behind the train tail decreases about 14.4%/10.7%/11.3% and 51%/31.5%/18% as the nose length increase to 7.4m and 9.4m respectively. As a result, increasing the length of the nose could reduce the magnitude and fluctuation of wake slipstream. However, this effect to reduce the wake velocity is weakened in the tunnel.

References

1. Howe, M., Iida, M., Fukuda, T. & Maeda, T., 2000. Theoretical and experimental investigation of the compression wave generated by a train entering a tunnel with a flared portal. *Journal of Fluid Mechanics,* pp. 111-132.

2. Chen, G. et al., 2019. Dynamic analysis of the effect of nose length on train aerodynamic performance. *Journal of Wind Engineering and Industrial Aerodynamics,* 184(2019), pp. 198-208.

3. Bell, J. et al., 2014. Wind tunnel analysis of the slipstream and wake of a high-speed train. *Journal of Wind Engineering and Industrial Aerodynamics,* pp. 122-138.

4. Baker, C. J. et al., 2001. The slipstream and wake of a high-speed train. *Proceedings of the Institution of Mechanical Engineers, Part F: Journal of Rail and Rapid Transit,* 215(2), pp. 83-99.

5. Sterling, M., Baker, C., Jordan, S. & Johnson, T., 2008. A study of the slipstreams of high-speed passenger trains and freight trains. *Proceedings of the Institution of Mechanical Engineers, Part F: Journal of Rail and Rapid Transit,* 222(2), pp. 177-193.

6. Tian, H., 2019. Review of research on high-speed railway aerodynamics in China. *Transportation Safety and Environment,* 1(1), pp. 1-21.

7. Baker, C. et al., 2014a. Full-scale measurement and analysis of train slipstreams and wakes. Part 1: Ensemble averages. *Proceedings of the Institution of Mechanical Engineers, Part F: Journal of Rail and Rapid Transit,* 228(5), pp. 451-467.

8. Huang, S., Hemida, H. & Yang, M., 2016. Numerical calculation of the slipstream generated by a CRH2 high-speed train. *Proceedings of the Institution of Mechanical Engineers, Part F: Journal of Rail and Rapid Transit,* 230(1), pp. 103-116.

9. Hemida, H. & Baker, C., 2012. The Calculation of Train Slipstreams using Large-Eddy Simulation. *Journal of Rail and Rapid Transit,* 228(1), pp. 25-36.

10. Flynn, D., Hemida, H., Soper, D. & Baker, C., 2014. Detached-eddy simulation of the slipstream of an operational freight train. *Journal of Wind Engineering and Industrial Aerodynamics,* Volume 132, pp. 1-12.

11. Soper, D., Baker, C. & Sterling, M., 2014. Experimental investigation of the slipstream development around a container freight train using a moving model facility. *Journal of Wind Engineering and Industrial Aerodynamics,* Volume 135, pp. 105-117.
12. Bell, J. et al., 2016. Dynamics of trailing vortices in the wake of a generic high-speed train. *Journal of Fluids and Structures,* Volume 65, pp. 238-256.
13. Bell, J. et al., 2017. The effect of tail geometry on the slipstream and unsteady wake structure of high-speed trains. *Experimental Thermal and Fluid Science,* Volume 83, pp. 215-230.
14. Hemida, H., & Krajnović, S., 2010. LES study of the influence of the nose shape and yaw angles on flow structures around trains. *Journal of Wind Engineering and Industrial Aerodynamics*, *98*(1), 34-46.
15. Mohebbi, M., & Rezvani, M. A., 2019. Analysis of the effects of lateral wind on a high speed train on a double routed railway track with porous shelters. *Journal of Wind Engineering and Industrial Aerodynamics*, 184, 116-127.
16. Rezvani, M. A., & Mohebbi, M., 2014. Numerical Calculations of Aerodynamic Performance an ATM Train at Crosswind Conditions. *Wind and Structures*, Vol. 18, No. 5, pp. 529-548.
17. Mohebbi, M., & Rezvani, M. A., 2018. The Impact of Air Fences Geometry on Air Flow around an ICE3 High Speed Train on a Double Line Railway Track with Exposure to Crosswinds. *JOURNAL OF APPLIED FLUID MECHANICS (JAFM*), 11(3), 743-754.
18. Mohebbi, M., & Safaee, A. M., 2021. The optimum model determination of porous barriers in high-speed tracks. *Proceedings of the Institution of Mechanical Engineers, Part F: Journal of Rail and Rapid Transit.*
19. Mohebbi, M., & Rezvani, M. A., 2018. Two-dimensional analysis of the influence of windbreaks on airflow over a high-speed train under crosswind using lattice Boltzmann method. *Proceedings of the Institution of Mechanical Engineers, Part F: Journal of Rail and Rapid Transit*, 232(3), 863-872.
20. Mohebbi, M., & Rezvani, M. A., 2018. Multi objective optimization of aerodynamic design of high speed railway windbreaks using Lattice Boltzmann Method and wind tunnel test results. *International Journal of Rail Transportation*, *6*(3), 183-201.
21. Suzuki, M., Ido, A., Sakuma, Y. & Kajiyama, H., 2008. Full-scale measurement and numerical simulation of flow around high-speed train in tunnel. *Journal of mechanical systems for transportation and logistics,* 1(3), pp. 281-292.
22. Fei, R. Z., Li, M. P., Wei, C. Y. & Wei , G. Y., 2014. Research of train wind characteristics in high-speed railway tunnel. *In Advanced Materials Research,* Volume 919, pp. 865-868.
23. Liu, T., Tian, H. & Liang, X., 2010. Aerodynamic effects caused by trains entering tunnels. *ournal of Transportation Engineering,* 136(9), pp. 846-853
24. Gilbert, T., Baker, C. & Quinn, A., 2013. Gusts caused by high-speed trains in confined spaces

and tunnels. *Journal of wind engineering and industrial aerodynamics,* Volume 121, pp. 39-48.
25. Jiang, Z. et al., 2019. Numerical prediction of the slipstream caused by the trains with different marshalling forms entering a tunnel. *Journal of Wind Engineering and Industrial Aerodynamics,* Volume 189, pp. 276-288.
26. Li, W. & Liu, T., 2017. Three-dimensional Characteristics of the Slipstream Induced by a High-Speed Train Passing through a Tunnel. *DEStech Transactions on Engineering and Technology Research,* Volume icia.
27. lliadis, P., Hemida, H. & Soper, D., 2019. Numerical simulations of the separated flow around a freight train passing through a tunnel using the sliding mesh technique. *Proceedings of the Institution of Mechanical Engineers, Part F: Journal of Rail and Rapid Transit,* 237(8), pp. 857-868.
28. Faramehr, S. & Hemida, H., 2016. Aerodynamics of Trains in Tunnels,. *in Proceedings of the Third International Conference on Railway Technology: Research, Development and Maintenance, Civil-Comp Press,* p. Paper 36.
29. Wang, S. et al., 2017. The performance of different turbulence models (URANS, SAS and DES) for predicting high-speed train slipstream. *Journal of Wind Engineering and Industrial Aerodynamics,,* Volume 165, pp. 46-57.
30. Khayrullina, A., Blocken, B., Janssen, W. & Straathof, J., 2015. CFD simulation of train aerodynamics: Train-induced wind conditions at an underground railroad passenger platform. *Journal of Wind Engineering and Industrial Aerodynamics,* Volume 139, pp. 100-110.
31. CEN, 2013. Railway Applications – Aerodynamics. Part 4: Requirements and Test Procedures for Aerodynamics on Open Track,. In: *CEN EN* . s.l.:s.n., pp. 14067-4.
32. Niu, J., Wang, Y., Zhang, L. & Yuan, Y., 2018. Numerical analysis of aerodynamic characteristics of high-speed train. *International Journal of Heat and Mass Transfer,* 127(2018), pp. 188-199.
33. Hemida, H. & Krajnović, S., 2008. LES study of the influence of a train-nose shape on the flow structures under cross-wind conditions. *Journal of fluids engineering,* 130(9), pp. 1-12.
34. Li, X., Chen, G., Zhou, D. & Chen, Z., 2019. Impact of Different Nose Lengths on Flow-Field Structure around a High-Speed Train. *Applied Sciences,* 9(21), p. 4573.
35. Mohebbi, M., & Rezvani, M. A., 2021. 2D and 3D numerical and experimental analyses of the aerodynamic effects of air fences on a high-speed train. *Wind and Structures*, *32*(6), 539-550.
36. Xia, C. et al., 2017. Effects of ground configurations on the slipstream and near wake of a high-speed train. *Journal of Wind Engineering and Industrial Aerodynamics,* Volume 168, pp. 177-189.
37. Liu, C, et al., 2017. Application of hybrid RANS/LES turbulence models in rotor-stator fluid machinery: a comparative study. *International Journal of Numerical Methods for Heat & Fluid Flow*, 27(12).
38. Shur, M., Spalart, P., Strelets, M. & Travin, A., 2008. A hybrid RANS-LES approach with

delayed-DES and wall-modelled LES capabilities. *International Journal of Heat and Fluid Flow,* 29(6), pp. 1638-1649.

39. Chen, X. & Zhang, X., 2013. High-Order Interface for Aeroacoustic Computation Using Overset Grid. *AIAA journal,* 51(2), pp. 519-523.

40. Wang, G. et al., 2014. An overset grid method for large eddy simulation of turbomachinery stages. *Journal of Computational Physics,* Volume 274, pp. 333-355.

41. Baker, C. et al., 2014b. Full-scale measurement and analysis of train slipstreams and wakes. Part 2 Gust analysis. *Proceedings of the Institution of Mechanical Engineers, Part F: Journal of Rail and Rapid Transit,* 228(5), pp. 468-480.

42. Baker, C., 2010. The flow around high speed trains. *Journal of Wind Engineering and Industrial Aerodynamics,* 6-7(277-298), p. 98.